The National Center for Atmospheric Research Community Climate Model: CCM3*

J. T. KIEHL, J. J. HACK, G. B. BONAN, B. A. BOVILLE, D. L. WILLIAMSON, AND P. J. RASCH

National Center for Atmospheric Research,+ Boulder, Colorado

(Manuscript received 12 May 1997, in final form 14 October 1997)

ABSTRACT

The latest version of the National Center for Atmospheric Research (NCAR) Community Climate Model (CCM3) is described. The changes in both physical and dynamical formulation from CCM2 to CCM3 are presented. The major differences in CCM3 compared to CCM2 include changes to the parameterization of cloud properties, clear sky longwave radiation, deep convection, boundary layer processes, and land surface processes. A brief description of each of these parameterization changes is provided. These modifications to model physics have led to dramatic improvements in the simulated climate of the CCM. In particular, the top of atmosphere cloud radiative forcing is now in good agreement with observations, the Northern Hemisphere winter dynamical simulation has significantly improved, biases in surface land temperatures and precipitation have been substantially reduced, and the implied ocean heat transport is in very good agreement with recent observational estimates. The improvement in implied ocean heat transport is among the more important attributes of the CCM3 since it is used as the atmospheric component of the NCAR Climate System Model. Future improvements to the CCM3 are also discussed.

1. Introduction

For the past 15 years, the National Center for Atmospheric Research (NCAR) Climate and Global Dynamics division has provided a comprehensive, three-dimensional global atmospheric model to the atmospheric sciences community for use in the analysis and understanding of the earth's global climate. Because of its widespread use, the model was designated a community tool and given the name Community Climate Model (CCM). The first version of this model, CCM0 (A and B), was described in Pitcher et al. (1983) and Williamson (1983). This development activity firmly established NCAR's commitment to provide a versatile, well-documented atmospheric general circulation model that would be suitable for climate studies by NCAR and university scientists. A more detailed discussion of the early history and philosophy of the CCM can be found in Anthes (1986). The second-generation community model, CCM1, was introduced in 1987, and included a number of significant changes to the model formulation, which were manifested in changes to the simulated climate.

The third generation of the CCM, CCM2, was released in 1992. This version was the product of a major effort to improve the physical representation of a wide range of key climate processes, including clouds and radiation, moist convection, the planetary boundary layer, and large-scale transport. The introduction of this model also marked a new philosophy with respect to implementation. The CCM2 code was entirely restructured so as to satisfy three major objectives: much greater ease of use, which included portability across a wide range of computational platforms; conformance to a plug-compatible physics interface standard; and the incorporation of single-job multitasking capabilities. The model is described in Hack et al. (1993), while the climate simulation of the model was documented in Hack et al. (1994) and Kiehl et al. (1994).

As with each new version of the CCM, the motivation for developing CCM3 originated with the desire to reduce systematic biases in the climate simulation of CCM2. The major biases were related to deficiencies in the top of atmosphere cloud radiative forcing, a weak stationary wave structure in Northern Hemisphere winter, an overly vigorous hydrologic cycle, and land surface temperature biases in local summer. As we show, many of the parameterization changes in CCM3 have considerably reduced these particular biases in the simulation. There are also certain aspects of the CCM3

* An electronic supplement to this article may be found on the CD-ROM accompanying this issue or at http://www.ametsoc.org/AMS.

+ The National Center for Atmospheric Research is sponsored by the National Science Foundation.

Corresponding author address: Dr. Jeffrey T. Kiehl, NCAR/CGD, P.O. Box 3000, Boulder, CO 80307-3000.
E-mail: jtkon@ucar.edu

simulation that have degraded when compared to CCM2; the overall quality of the simulation is markedly improved.

The purpose of this study is to document the changes in physical parameterizations and numerical formulations in the CCM3 and compare the climate simulation of CCM3 to that produced by CCM2. Detailed comparisons of the climate simulation of CCM3 to various observations and analyses are provided by Hurrell et al. (1998) for the dynamical simulation, Hack et al. (1998) for the hydrologic and thermodynamic simulation, and Kiehl et al. (1998) for the energy budget simulation. The CCM3 is also the atmospheric component of the NCAR Climate System Model (CSM). The simulations of the fully coupled model are described in Boville and Gent (1998).

This study is organized as follows: section 2 describes the physical and dynamical processes that have changed from CCM2 to CCM3, section 3 presents comparisons of various climate metrics between CCM3 and CCM2, section 4 summarizes the major changes to CCM3 and discusses future improvements to the CCM3.

2. Description of changes from CCM2 to CCM3

A detailed description of both the physical parameterizations and numerical methods employed in the CCM3 is presented in Kiehl et al. (1996). A users' guide that describes how to run and alter the CCM3 is provided by Acker et al. (1996).

The CCM3 is a global spectral model with a horizontal T42 spectral resolution (approximately 2.8° × 2.8° transform grid). The model has 18 levels in the vertical with the model top at 2.9 mb. The model time step for this resolution is 20 min. The horizontal and vertical resolution of CCM3 is identical to that used in CCM2. The model includes a diurnal cycle, where radiative fluxes are calculated every hour. Between hourly calculations, the radiative fluxes are held fixed. The CCM3 includes a detailed physical model for land surface processes, called the Land Surface Model (LSM), which is described in Bonan (1998). The CCM3 also includes an optional thermodynamic slab ocean and sea ice model (SOM), which is useful for climate change studies. Here we describe the major differences between CCM3 and CCM2 with regard to physical and dynamical formulations.

a. Cloud parameterization

The changes to the parameterization of clouds in CCM3 can be grouped in terms of three processes: cloud fraction, cloud microphysics, and cloud radiative properties.

Cloud fraction is evaluated via a diagnostic method in CCM3. Although the basic approach is similar to that of the CCM2, the specific techniques represent significant changes to the collection of model physics. The diagnosis of cloud fraction represents a generalization of the scheme introduced by Slingo (1987) and depends on relative humidity; vertical pressure velocity, ω; atmospheric stability; and the convective mass flux associated with parameterized moist convection. Three types of cloud are diagnosed by the scheme: convective cloud, layered cloud, and low-level marine stratus. Some of the major changes from Slingo (1987) are the following: clouds are allowed to form in any model layer, except the layer nearest the surface; low-level frontal clouds occur for all vertical velocities, $\omega < \omega_c$ (where ω_c is an arbitrary threshold); the relative humidity thresholds for mid- and upper-level-layered clouds are functions of atmospheric stability; and convective cloud amount is determined from the rate of convective overturning (as opposed to convective precipitation rate). The minimum convective cloud fraction requirement of 20% employed in the CCM2 has been removed.

Total column convective cloud amount is diagnosed from the presence and strength of moist convective activity. In particular, it is a function of the column-averaged convective mass flux diagnosed by the moist convective parameterization (e.g., along the lines of Xu and Krueger 1991), where

$$\overline{A}_{\text{conv}} = 0.035 \ln(1.0 + \overline{M_c}), \tag{1}$$

where the vertically averaged convective mass flux $\overline{M_c}$ is given by

$$\overline{M_c} = \int_{p_T}^{p_s} m_c(p)\, dp \Big/ \int_{p_T}^{p_s} dp, \tag{2}$$

$m_c(p)$ is in units of mb day^{-1} and $\overline{A}_{\text{conv}}$ is not allowed to exceed 80%. The convective cloud amount in each model layer is assumed to be randomly overlapped within the convectively active region, the bounds of which are provided by the moist convection parameterization. This formulation produces a more realistic distribution of convective cloud cover, particularly for nonprecipitating convective regimes, and eliminates the need to impose a minimum convective cloud fraction for nonprecipitating conditions. This change to diagnosing convective cloud amount helped to improve the CCM2 albedo bias in the subtropics.

The cloud microphysics in CCM3, although an improvement over that used in CCM2, is still based on a simple formalism, which includes total cloud condensate path and cloud particle size information for the radiation model. Thus, the approach is purely diagnostic as opposed to the more complex fully prognostic approach. As in CCM2, cloud condensate is vertically distributed according to a liquid water scale-height cloud water concentration:

$$\rho_l = \rho_l^0 e^{(-z/h_l)}, \tag{3}$$

where the reference value ρ_l^0 is equal to 0.21 g m^{-3}. CCM2 employed a zonally symmetric meridional de-

pendence for the cloud water scale height, whereas in CCM3 the liquid water scale height, h_l, is locally diagnosed as a function of the vertically integrated water vapor (precipitable water):

$$h_l = a \ln\left(1.0 + \frac{b}{g}\int_{p_T}^{p_s} q\, dp\right), \tag{4}$$

where the parameters have been empirically determined to be $a = 700$ m and $b = 1$ m^2 kg^{-1}. This approach extends the CCM2 cloud water framework using a simple empirical thermodynamic argument allowing cloud water path to vary in both the horizontal and vertical directions. The sensitivity of the CCM2 climate to this diagnostic cloud water scheme is discussed in Hack (1998a).

The other cloud microphysics property that is employed within the CCM3 is the cloud droplet size. This property directly affects the cloud radiative properties. Observational studies have shown a distinct difference between maritime and continental effective cloud drop size, r_e, for warm clouds. For this reason, the CCM3 differentiates between the cloud drop effective radius for clouds diagnosed over maritime and continental regimes (Kiehl 1994). Over the ocean, the cloud drop effective radius for liquid water clouds, r_{el}, is specified to be 10 μm, as in the CCM2. Over landmasses r_{el} is determined using

$$r_{el} = \begin{cases} 5\ \mu\text{m} & T > -10°\text{C} \\ 5 - 5\left(\dfrac{T+10}{20}\right)\mu\text{m} & -30°\text{C} \le T \le -10°\text{C} \\ r_{ei} & T < -30°\text{C}. \end{cases} \tag{5}$$

Dandin et al. (1997) have shown that (5) is a reasonable approximation for the continental-scale variation in cloud particle size. An ice particle effective radius, r_{ei}, is also diagnosed by CCM3, which at the moment amounts to a specification of ice radius as a function of normalized pressure:

$$r_{ei} = \begin{cases} 10\ \mu\text{m} & p/p_s > p_I^{low} \\ r_{ei}^{max} - (r_{ei}^{max} - r_{ei}^{min})\left[\dfrac{(p/p_s - p_I^{low})}{p_I^{high} - p_I^{low}}\right]\mu\text{m} & \\ & p/p_s \le p_I^{high}, \end{cases} \tag{6}$$

where $r_{ei}^{max} = 30$ μm, $r_{ei}^{min} = 10$ μm, $p_I^{high} = 0.4$, and $p_I^{low} = 0.0$.

The fraction of the total cloud water in the form of ice particles is then determined using

$$f_{ice} = \begin{cases} 0 & T > -10°\text{C} \\ -0.05(T+10) & -30°\text{C} \le T \le -10°\text{C} \\ 1 & T < -30°\text{C}, \end{cases} \tag{7}$$

which is based on observations presented in Rogers and Yau (1989). Note the exact limits of the transitions between complete liquid phase and complete ice phase requires further study (e.g., Zender and Kiehl 1997).

Cloud radiative properties also explicitly account for the phase of water. For shortwave radiation we use the expressions of Slingo (1989) for liquid water clouds. The cloud liquid optical properties, for each spectral interval (extinction optical depth, single-scattering albedo, asymmetry parameter, and forward-scattering parameter), are defined in terms of the liquid water path and effective drop size (see Briegleb 1992).

The radiative properties of ice cloud in the shortwave spectral region are defined by

$$\tau_i^c = \text{CWP}\left[a_i^i + \frac{b_i^i}{r_{ei}}\right] f_{ice} \tag{8}$$

$$\omega_i^c = 1 - c_i^i - d_i^i r_{ei} \tag{9}$$

$$g_i^c = e_i^i + f_i^i r_{ei} \tag{10}$$

$$f_i^c = (g_i^i)^2, \tag{11}$$

where the subscript i denotes ice radiative properties. The values for the coefficients a–f are based on the results of Ebert and Curry (1992). The bulk optical properties are computed using the approach of Cess (1985). Thus, given the liquid water path and the effective cloud particle size, the cloud radiative properties are fully determined for the CCM3.

In the longwave spectral region, the cloud emissivity is accounted for by defining an effective cloud amount for each model layer:

$$A_c' = \epsilon_{cld} A_c, \tag{12}$$

where A_c is the model diagnosed cloud fraction in a layer. The cloud emissivity is defined as (Liou 1992):

$$\epsilon_{cld} = 1 - e^{-D\kappa_{abs}\text{CWP}}, \tag{13}$$

where D is a diffusivity factor set to 1.66 (Stephens 1984; Liou 1992), κ_{abs} is the longwave absorption coefficient (m^2 g^{-1}), and CWP is the cloud water path (gm^{-2}). The absorption coefficient is defined as a weighted average between liquid and ice phase:

$$\kappa_{abs} = \kappa_l(1 - f_{ice}) + \kappa_i f_{ice}, \tag{14}$$

where κ_l is the longwave absorption coefficient for liquid cloud water and has a value of 0.090361, such that $D\kappa_l$ is 0.15, which is in the range of observations and theory (e.g., Stephens 1984). Here, κ_i is the absorption coefficient for ice clouds and is based on a broadband fit to the emissivity given by Ebert and Curry's formulation:

$$\kappa_i = 0.005 + \frac{1}{r_{ei}}. \tag{15}$$

b. Moist convective parameterizations

Moist convection in the CCM3 now includes the deep convection scheme developed by Zhang and McFarlane (1995), which operates in conjunction with the scheme of Hack (1994). The deep scheme is based on a plume ensemble approach where it is assumed that an ensemble of convective-scale updrafts (and the associated saturated downdrafts) may exist whenever the atmosphere is conditionally unstable in the lower troposphere. The updraft ensemble is composed of plumes sufficiently buoyant so as to penetrate the unstable layer, where all plumes have the same upward mass flux at the bottom of the convective layer. Moist convection occurs only when there is convective available potential energy (CAPE) for which parcel ascent from the subcloud layer acts to destroy the CAPE at an exponential rate using a specified adjustment timescale.

The large-scale budget equations distinguish between a cloud and subcloud layer where the temperature and moisture response to convection in the cloud layer is written in terms of bulk convective fluxes. In the cloud layer these equations take the form

$$c_p\left(\frac{\partial T}{\partial t}\right)_{cu} = -\frac{1}{\rho}\frac{\partial}{\partial z}(M_u S_u + M_d S_d - M_c S) + L(C - E), \tag{16}$$

$$\left(\frac{\partial q}{\partial t}\right)_{cu} = -\frac{1}{\rho}\frac{\partial}{\partial z}(M_u q_u + M_d q_d - M_c q) + E - C. \tag{17}$$

The cloud model is composed of two components, the updraft ensemble and the downdraft ensemble. The updraft ensemble is represented as a collection of entraining plumes, each with a characteristic fractional entrainment rate. Mass carried upward by the plumes is detrained into the environment in a thin layer at the top of the plume where the detrained air is assumed to have the same thermal properties as in the environment. The top of the shallowest of the convective plumes is assumed to be no lower than the midtropospheric minimum in saturated moist static energy, h^*, ensuring that the cloud-top detrainment is confined to the conditionally stable portion of the atmospheric column. Each plume is assumed to have the same value for the cloud-base mass flux where the vertical distribution of the cloud updraft mass flux is given by

$$M_u = M_b \int_0^{\lambda_D} \frac{1}{\lambda_0} e^{\lambda(z - z_m)}\, d\lambda, \tag{18}$$

where λ_0 is the maximum detrainment rate, and λ_D is the entrainment rate for the updraft that detrains at height z, which is iteratively determined by requiring that

$$h_b - h^* = \lambda_D \int_{z_m}^{z} [h_b - h(z')] e^{[\lambda_D(z' - z)]}\, dz'. \tag{19}$$

Downdrafts are assumed to exist whenever there is precipitation production in the updraft ensemble where the downdrafts start at or below the bottom of the updraft detrainment layer. Detrainment from the downdrafts is confined to the subcloud layer. The ensemble downdraft mass flux takes a similar form to (18) and includes a ''proportionality factor,'' which ensures that the downdraft strength is physically consistent with precipitation availability. This coefficient takes the form

$$\alpha = \mu\left[\frac{P}{P + E_d}\right], \tag{20}$$

where P is the total precipitaion in the convective layer and E_d is the rainwater evaporation required to maintain the downdraft in a saturated state.

The parameterization is closed—that is, the cloud base mass fluxes are determined—as a function of the rate at which the cumulus consume CAPE. Since the large-scale temperature and moisture changes in both the cloud and subcloud layer are linearly proportional to the cloud-base updraft mass flux, the CAPE change due to convective activity can be written as

$$\left(\frac{\partial A}{\partial t}\right)_{cu} = -M_b F, \tag{21}$$

where F is the CAPE consumption rate per unit cloud-base mass flux. The closure condition is that the CAPE is consumed at an exponential rate by cumulus convection with a characteristic adjustment timescale τ;

$$M_b = \frac{A}{\tau F}. \tag{22}$$

Following the application of the deep convective parameterization, the scheme developed by Hack (1994) is applied to deal with shallow- and midlevel convection. The diabatic and convective transport tendencies from the two schemes are summed and represent the collective effect of moist convection. The principal climate response to this hybrid approach is a warmer tropical tropopause, a smoother distribution of tropical precipitation, and substantially reduced latent heat fluxes in the vicinity of deep convection. Additional analysis of the deep convection parameterization behavior in CCM3 can be found in Zhang et al. (1998).

c. Radiation

There are two major changes in the radiation model between CCM3 and CCM2. In the longwave spectral region, CCM3 now includes the radiative effects of the following trace gases: CH_4, N_2O, CFC11, and CFC12. The model also accounts for the radiative properties for

two weak CO_2 bands located at 9.4 and 10.4 μm. The addition of these gases to the longwave scheme in the CCM required major changes to the model to account for the overlap effect among various absorbers. A detailed description of the parameterization of the trace gases for CCM3 is found in Kiehl et al. (1996). The following is a brief description of how the trace gases are implemented in the CCM3.

The method employed in the CCM3 to represent longwave radiative transfer is based on an absorptivity–emissivity formulation (Ramanathan and Downey 1986). Downward and upward fluxes at pressure level p are given by

$$F^{\downarrow}(p) = B(0)\epsilon(0, p) + \int_0^p \alpha(p, p')\, dB(p') \quad (23)$$

$$F^{\uparrow}(p) = B(T_s) - \int_p^{p_s} \alpha(p, p')\, dB(p'), \quad (24)$$

where $B(T) = \sigma T^4$ is the Stefan–Boltzmann relation and α and ϵ are the absorptivity and emissivity, respectively:

$$\alpha(p, p') = \frac{\int_0^{\infty} [dB_\nu(p')/dT(p')][1 - \mathcal{T}_\nu(p, p')]\, d\nu}{dB(p')/dT(p')} \quad (25)$$

$$\epsilon(0, p) = \frac{\int_0^{\infty} B_\nu(\mathcal{T}_\infty)[1 - \mathcal{T}_\nu(0, p)]\, d\nu}{B(0)}, \quad (26)$$

where the integration is over wavenumber, ν. Here $B_\nu(p)$ is the Planck function and $\mathcal{T}_\nu$ is the atmospheric transmission. Thus, to solve for fluxes at each model layer, we need solutions to the following:

$$\int_0^{\infty} (1 - \mathcal{T}_\nu)F(B_\nu)\, d\nu, \quad (27)$$

where $F(B_\nu)$ is the Planck function for the emissivity, or the derivative of the Planck function with respect to temperature for the absorptivity.

The general method employed for the solution of (27) for a given gas is based on the broadband model approach described by Kiehl and Briegleb (1991) and Kiehl and Ramanathan (1983), which is based on the earlier work of Ramanathan (1976). The broadband approach assumes that the spectral range of absorption by a gas is limited to a relatively small range in wavenumber, ν, and hence, can be evaluated at the band center; that is,

$$\int_{\nu_1}^{\nu_2} (1 - \mathcal{T}_\nu)F(B_\nu)\, d\nu \approx F(B_{\bar{\nu}}) \int_{\nu_1}^{\nu_2} (1 - \mathcal{T}_\nu)\, d\nu = F(B_{\bar{\nu}})A, \quad (28)$$

where A is the band absorptance (or equivalent width) per centimeter. Note that A, in general, is a function of the absorber amount, the local emitting temperature, and the pressure. Thus, the broadband model is based on finding analytic expressions for the band absorptance. Ramanathan (1976) proposed the following functional form for A:

$$A(u, T, P) = 2A_0 \ln\left[1 + \frac{u}{\sqrt{4 + u(1 + 1/\beta)}}\right], \quad (29)$$

where A_0 is an empirical constant, u is the scaled dimensionless pathlength:

$$u = \int \frac{S(T)}{A_0(T)} \mu\rho_a\, dz, \quad (30)$$

where $S(T)$ is the band strength, μ is the mass mixing ratio of the absorber, and ρ_a is the density of air. Here β is a line-width factor:

$$\beta = \frac{4}{ud} \int \gamma(T)\left(\frac{P}{P_0}\right) du, \quad (31)$$

where $\gamma(T)$ is the mean line halfwidth for the band, P is the atmospheric pressure, and P_0 is a reference pressure and d is the mean line spacing for the band. The determination of γ, d, S from spectroscopic line databases, such as the FASCODE database, is described in detail in Kiehl and Ramanathan (1983). Kiehl and Briegleb (1991) describe how (29) can be extended to account for subbands within a spectral region. Essentially, the argument in the log function is replaced by a summation over the subbands. This broadband formalism is employed for CO_2, O_3, CH_4, N_2O, and minor absorption bands of CO_2, whereas for the CFCs we employ the exponential transmission approximation discussed by Ramanathan et al. (1985):

$$T = \exp\{-D[S(T)/\Delta\nu]W\}, \quad (32)$$

where $\Delta\nu$ is the bandwidth and W is the absorber pathlength:

$$W = \int \mu\rho_a\, dz, \quad (33)$$

and D is a diffusivity factor. The final aspect that must be incorporated into the broadband method is the overlap of one or more absorbers within the same spectral region. Thus, for the wavenumber range of interest—namely, 500 to 1500 cm^{-1}—the radiative flux is determined in part by the integral:

$$\int_{500}^{1500} (1 - \mathcal{T}_\nu)F(B_\nu)\, d\nu, \quad (34)$$

which can be reformulated for given subintervals in wavenumbers as

$$\int_{500}^{1500} (1 - \mathcal{T}_\nu) F(B_\nu)\, d\nu$$
$$= \int_{500}^{750} (1 - \mathcal{T}^1_{CO_2}\mathcal{T}^1_{N_2O}\mathcal{T}_{H_2O}) F(B_\nu)\, d\nu + \int_{750}^{820} (1 - \mathcal{T}^1_{CFC11}\mathcal{T}_{H_2O}) F(B_\nu)\, d\nu$$
$$+ \int_{820}^{880} (1 - \mathcal{T}^2_{CFC11}\mathcal{T}_{H_2O}) F(B_\nu)\, d\nu + \int_{880}^{900} (1 - \mathcal{T}^1_{CFC12}\mathcal{T}_{H_2O}) F(B_\nu)\, d\nu$$
$$+ \int_{900}^{1000} (1 - \mathcal{T}^2_{CO_2}\mathcal{T}_{H_2O}\mathcal{T}^3_{CFC11}\mathcal{T}^2_{CFC12}) F(B_\nu)\, d\nu + \int_{1000}^{1120} (1 - \mathcal{T}^3_{CO_2}\mathcal{T}_{O_3}\mathcal{T}_{H_2O}\mathcal{T}^4_{CFC11}\mathcal{T}^3_{CFC12}) F(B_\nu)\, d\nu$$
$$+ \int_{1120}^{1170} (1 - \mathcal{T}^4_{CFC12}\mathcal{T}_{H_2O}\mathcal{T}^2_{N_2O}) F(B_\nu)\, d\nu + \int_{1170}^{1500} (1 - \mathcal{T}_{CH_4}\mathcal{T}^3_{N_2O}\mathcal{T}_{H_2O}) F(B_\nu)\, d\nu, \quad (35)$$

where superscripts denote a specific absorption band for a given gas. The subintervals, in turn, can be reformulated in terms of the absorptance for a given gas and the ''overlap'' transmission factors that multiply this transmission. Note that in the broadband formulation there is an explicit assumption that these two are uncorrelated (see Kiehl and Ramanathan 1983). The specific parameterizations for each of these subintervals depends on spectroscopic data particular to a given gas and absorption band for that absorber. Details of the parameterization for each trace gas are provided in Kiehl et al. (1996).

The distribution of CH_4, N_2O, and CFCs is specified in terms of zonal-mean mixing ratios for each species. In the troposphere, the mixing ratio for each gas is constant in pressure up to fixed tropopause pressure of

$$p_{trop} = 250.0 - 150.0 \cos^2\phi \text{ mb}, \quad (36)$$

where ϕ is latitude. The tropospheric mixing ratios are specified at the 1992 levels based on the 1994 International Panel on Climate Change report. For pressures less than p_{trop}, each trace gas mixing ratio decreases with a specified scale height, which was determined from results of a two-dimensional chemical transport model (S. Solomon 1996, personal communication). These stratospheric scale heights linearly depend on latitude to provide a more realistic zonal distribution of trace gas mixing ratios. The functional form of the parameterization is given in Kiehl et al. (1996).

In the shortwave spectral region, CCM3 employs the δ-Eddington method used in CCM2 (Briegleb 1992). However, a uniform (in space and time) background boundary layer aerosol is now included in CCM3. The aerosol is well mixed in the bottom three layers of the model. The aerosol mass mixing ratio in these layers is specified to yield a visible optical depth of 0.14. We view this prescription of aerosol as a ''place holder'' for future implementations of various aerosol types that have realistic spatial and temporal variability. The optical properties of the aerosol are identical to sulfate aerosols described by Kiehl and Briegleb (1993).

d. Surface and boundary layer formulation

The CCM3 continues to make use of a ''nonlocal'' formulation for atmospheric boundary layer (ABL) transport (Holtslag and Boville 1993). The nonlocal transport term in this formulation represents nonlocal influences on the mixing by turbulence (Deardorff 1972), which is small under stable conditions. For unstable conditions, however, most heat and moisture transport is achieved by turbulent eddies with sizes on the order of the depth h of the ABL. Accordingly, the formulations of the eddy diffusivity and the nonlocal terms are dependent on the boundary layer height h. The CCM2 configuration of this nonlocal scheme made use of a traditional approach to estimating the boundary layer depth by assuming a constant value for the bulk Richardson number across the boundary layer depth, so that h was iteratively determined using

$$h = \frac{\text{Ri}_{cr}[u(h)^2 + v(h)^2]}{(g/\theta_s)[\theta_v(h) - \theta_s]}, \quad (37)$$

where Ri_{cr} is a critical bulk Richardson number for the ABL, $u(h)$ and $v(h)$ are the horizontal velocity components at h, g/θ_s is the buoyancy parameter, and $\theta_v(h)$ is the virtual temperature at h. The quantity θ_s is a measure of the surface air temperature, which under unstable conditions was given by

$$\theta_s = \theta_v(z_s) + b\frac{(\overline{w'\theta'_v})_s}{w_m}, \quad (38)$$

where b is a free parameter, $(\overline{w'\theta'_v})_s$ is the virtual heat flux at the surface, $\theta_v(z_s)$ is a virtual temperature in the atmospheric surface layer (nominally 10 m), $b\,(\overline{w'\theta'_v})_s/w_m$ represents a temperature excess (a measure of the strength of convective thermals in the lower part of the

ABL), and unstable conditions are determined by $(\overline{w'\theta'_v})_s > 0$. The quantity $\theta_v(z_s)$ was calculated from the temperature and moisture of the first model level and of the surface by applying the procedure in Geleyn (1988). The value of the critical bulk Richardson number Ri_{cr}, which generally depends on the vertical resolution of the model, was chosen as $Ri_{cr} = 0.5$ for the CCM2.

Vogelezang and Holtslag (1996) have recently studied the suitability of this formulation in the context of field observations, large-eddy simulations (Moeng and Sullivan 1994), and an $E - \epsilon$ turbulence closure model (Duynkerke 1988). They propose a revised formulation that combines shear production in the outer region of the boundary layer with surface friction, where the Richardson number estimate is based on the differences in wind and virtual temperature between the top of the ABL and a lower height that is well outside the surface layer (i.e., 20–80 m). In addition to providing more realistic estimates of boundary layer depth, the revised formulation provides a smoother transition between stable and neutral boundary layers. Consequently, CCM3 employs the Vogelezang and Holtslag (1996) formulation for estimating the atmospheric boundary layer height, which can be written as

$$h = z_s + \frac{\mathrm{Ri}_{cr}\{[u(h) - u_{SL}]^2 + [v(h) - v_{SL}]^2 + \mathcal{B}u_*^2\}}{(g/\theta_{SL})[\theta_v(h) - \theta_{SL}]}. \quad (39)$$

The quantities u_{SL}, v_{SL}, and θ_{SL} represent the horizontal wind components and virtual potential temperature just above the surface layer (nominally $0.1h$). In practice, the lowest model level values for these quantities are used to iteratively determine h for all stability conditions, where the critical Richardson number, Ri_{cr}, is assumed to be 0.3. The parameter $\mathcal{B}$ has been experimentally determined to be equal to 100 (see Vogelezang and Holtslag 1996). The computation starts by calculating the bulk Richardson number Ri between the level of θ_{SL} and subsequent higher levels of the model. Once Ri exceeds the critical value, the value of h is derived by linear interpolation between the level with $Ri > Ri_{cr}$ and the level below.

This change results in a much better estimates of ABL height that translates into an important repartitioning of the turbulent surface heat flux from latent energy to sensible energy. The reduction in latent heat flux is on the order of 8 W m^{-2} in the global annual mean, representing the largest component of the overall reduction in the magnitude of the simulated hydrologic cycle.

The bulk formulas used to determine the turbulent fluxes of momentum (stress), water (evaporation, or latent heat), and sensible heat into the atmosphere over ocean and ice surfaces are

$$(\boldsymbol{\tau}, E, H) = \rho_A|\Delta\mathbf{v}|(C_D\Delta\mathbf{v}, C_E\Delta q, C_pC_H\Delta\theta), \quad (40)$$

where ρ_A is atmospheric surface density and C_p is the specific heat. Since CCM3 does not allow for motion of either the ocean or ice surfaces, the velocity difference between surface and atmosphere is $\Delta\mathbf{v} = \mathbf{v}_A$, the velocity of the lowest model level. The potential temperature difference is $\Delta\theta = \theta_A - T_s$, where T_s is the surface temperature. The specific humidity difference is $\Delta q = q_A - c_1c_2 \exp(c_3/T_s)/\rho_A$, where $c_1 = 0.98$ over oceans (accounting for the salinity of seawater) and $c_1 = 1$ over ice, $c_2 = 640\,380$ kg m^{-3}, and $c_3 = -5107.4$ K.

In (40), the transfer coefficients between either ocean or ice surfaces and the atmosphere are computed at a height Z_A and are functions of the stability, ζ:

$$C_{(D,E,H)} = \kappa^2\left[\ln\left(\frac{Z_A}{Z_{0m}}\right) - \psi_m\right]^{-1}\left[\ln\left(\frac{Z_A}{Z_{0(m,e,h)}}\right) - \psi_{(m,s,s)}\right]^{-1}, \quad (41)$$

where $\kappa = 0.4$ is von Kármán's constant and $Z_{0(m,e,h)}$ is the roughness length for momentum, evaporation, or heat, respectively. The integrated flux profiles, ψ_m for momentum and ψ_s for scalars, under stable conditions ($\zeta > 0$) are

$$\psi_m(\zeta) = \psi_s(\zeta) = -5\zeta. \quad (42)$$

For unstable conditions ($\zeta < 0$), the flux profiles are

$$\psi_m(\zeta) = 2\ln[0.5(1 + X)] + \ln[0.5(1 + X^2)] - 2\tan^{-1}X + 0.5\pi, \quad (43)$$

$$\psi_s(\zeta) = 2\ln[0.5(1 + X^2)], \quad (44)$$

$$X = (1 - 16\zeta)^{1/4}. \quad (45)$$

The stability parameter used in (42)–(45) is

$$\zeta = \frac{\kappa g Z_A}{u^{*2}}\left(\frac{\theta^*}{\theta_v} + \frac{Q^*}{(\epsilon^{-1} + q_A)}\right), \quad (46)$$

where the virtual potential temperature is $\theta_v = \theta_A(1 + \epsilon q_A)$; q_A and θ_A are the lowest level atmospheric humidity and potential temperature, respectively; and $\epsilon = 0.606$. The turbulent velocity scales in (46) are

$$u^* = C_D^{1/2}|\Delta\mathbf{v}|,$$

$$(Q^*, \theta^*) = C_{(E,H)}\frac{|\Delta\mathbf{v}|}{u^*}(\Delta q, \Delta\theta). \quad (47)$$

The roughness lengths over sea ice are all assumed to be equal: $Z_{0m} = Z_{0e} = Z_{0h} = 0.04$ m. Over oceans, $Z_{0e} = 9.5 \times 10^{-5}$ m under all conditions and $Z_{0h} = 2.2 \times 10^{-9}$ m for $\zeta > 0$, $Z_{0h} = 4.9 \times 10^{-5}$ m for $\zeta \le 0$, which are given in Large and Pond (1982). The momentum roughness length depends on the wind speed evaluated at 10 m as

$$Z_{0m} = 10\exp - \left[\kappa\left(\frac{c_4}{U_{10}} + c_5 + c_6U_{10}\right)^{-1}\right],$$

$$U_{10} = U_A\left[1 + \frac{\sqrt{C_{10}^N}}{\kappa}\ln\left(\frac{Z_A}{10} - \psi_m\right)\right]^{-1}, \quad (48)$$

where $c_4 = 0.0027$ m s^{-1}, $c_5 = 0.000142$, $c_6 = 0.0000764$ m^{-1} s, and the required drag coefficient at 10-m height and neutral stability is $C_{10}^{N} = c_4 U_{10}^{-1} + c_5 + c_6 U_{10}$ as given by Large et al. (1994).

The transfer coefficients in (40) and (41) depend on the stability following (42)–(45), which itself depends on the surface fluxes (46) and (47). The transfer coefficients also depend on the momentum roughness, which itself varies with the surface fluxes over oceans (48). The above system of equations is solved by iteration.

e. Dynamical formulation

The discrete vertical approximations in CCM3 have been changed to those of Williamson and Olson (1994), which maintain the energy conservation characteristics of CCM2 but add the property that the discrete pressure vertical velocity ω is consistent with the discrete continuity equation. In this system the global integral of ω on those model levels that are pure pressure surfaces is zero as it should be, unlike in the CCM2 system. As in CCM2, CCM3 adopts a hybrid vertical coordinate (η) defined by

$$p(\eta, p_s) = A(\eta)p_o + B(\eta)p_s, \tag{49}$$

where p is pressure, p_s is surface pressure, and p_o is a specified constant reference pressure. In this η system the continuity equation is

$$\frac{\partial B}{\partial \eta}\left(\frac{\partial \ln p_s}{\partial t} + \mathbf{V}\cdot\boldsymbol{\nabla}\ln p_s\right) = -\left(\frac{\partial p}{\partial \eta}\right)\frac{1}{p_s}\delta - \frac{1}{p_s}\frac{\partial}{\partial \eta}\left(\dot{\eta}\frac{\partial p}{\partial \eta}\right), \tag{50}$$

where $\mathbf{V}$ is the horizontal vector velocity and δ is the horizontal divergence. Integration from the top of the atmosphere to the bottom gives the prognostic equation for $\ln p_s$:

$$\ln p_s^{n+1} = \ln p_s^{n-1} - 2\Delta t\frac{1}{p_s^n}\sum_{l=1}^{K}(\delta_l^n \Delta p_l^n + \mathbf{V}_l^n \cdot p_s^n \boldsymbol{\nabla}\ln p_s^n \Delta B_l)$$

$$-2\Delta t\sum_{l=1}^{K}\left(\frac{\delta_l^{n-1} + \delta_l^{n+1}}{2} - \delta_l^n\right)\frac{1}{p_s^r}\Delta p_l^r, \tag{51}$$

where n denotes the time level, K is the number of vertical layers, Δp_l is the pressure thickness of layer l, and superscript r denotes a reference atmosphere about which the semi-implicit linearization takes place. Integration from the top of the atmosphere to a model-layer interface gives the approximation for the η vertical velocity:

$$\left(\dot{\eta}\frac{\partial p}{\partial \eta}\right)_{k+1/2} = B_{k+1/2}\sum_{l=1}^{K}(\delta_l \Delta p_l + \mathbf{V}_l \cdot p_s \boldsymbol{\nabla}\ln p_s \Delta B_l)$$

$$-\sum_{l=1}^{k}(\delta_l \Delta p_l + \mathbf{V}_l \cdot p_s \boldsymbol{\nabla}\ln p_s \Delta B_l). \tag{52}$$

By definition, the vertical velocity ω is related to $\ln p_s$ and $\dot{\eta}$ by

$$\frac{\omega}{p} = \frac{p_s}{p}\left[B(\eta)\left(\frac{\partial \ln p_s}{\partial t} + \mathbf{V}\cdot\boldsymbol{\nabla}\ln p_s\right) + \frac{1}{p_s}\dot{\eta}\frac{\partial p}{\partial \eta}\right]. \tag{53}$$

A discrete pressure vertical velocity ω of the form

$$\left(\frac{\omega}{p}\right)_k = \frac{p_s}{p_k}B_k \mathbf{V}_k \cdot \boldsymbol{\nabla}\ln p_s$$

$$-\sum_{l=1}^{k} C_{kl}(\delta_l \Delta p_l + \mathbf{V}_l \cdot p_s \boldsymbol{\nabla}\ln p_s \Delta B_l) \tag{54}$$

is consistent with the discrete ($\dot{\eta}\partial p/\partial \eta$) and the explicit component of the surface pressure tendency equation ($\ln p_s^{n+1} - \ln p_s^{n-1}$)/$2\Delta t$ if the integration matrix $\mathbf{C}_{kl}$ is defined by

$$\mathbf{C}_{kl} = \begin{cases} \dfrac{1}{p_k} & \text{for } l < k \\ \dfrac{1}{2p_k} & \text{for } l = k, \end{cases} \tag{55}$$

and

$$B_k = \frac{1}{2}(B_{k+1/2} + B_{k-1/2}). \tag{56}$$

Finally, for energy conservation, the integration matrix $\mathbf{H}_{kl}$ in the hydrostatic equation,

$$\Phi_k = \Phi_s + \mathbf{R}\sum_{l=k}^{K}\mathbf{H}_{kl}(p)\mathbf{T}_{v_l}, \tag{57}$$

is defined from the matrix $\mathbf{C}_{kl}$ by

$$\mathbf{H}_{kl} = \mathbf{C}_{lk}\Delta p_l. \tag{58}$$

For details of the derivations see Williamson and Olson (1994) and for complete specification of the model equations see Kiehl et al. (1996).

The orographic gravity wave drag included in CCM3 is similar to the McFarlane (1987) parameterization in CCM2. Vertically propagating, but horizontally stationary, gravity waves forced by flow over subgrid-scale orography are parameterized in terms of the surface stress generated. The gravity wave stress is conserved in the vertical unless the stress exceeds a ''saturation'' value that is a function of the background (resolved) state and the specified wave parameters.

The saturation condition, following McFarlane (1987), is given by a maximum streamline slope associated with the waves superimposed on the resolved flow, represented by a critical Froude number, F_c. The maximum stress that can be carried in the gravity waves is then

$$\tau(z) \le \tau_{sat}(z) = F_c^2 E\frac{k}{2}\rho\frac{|\overline{u}|^3}{N}, \tag{59}$$

where τ_{sat} is the saturation stress, E is an empirical ''ef-

ficiency factor,'' k is the horizontal wavenumber, ρ is the resolved-scale density, and N is the resolved-scale Brunt–Väisällä frequency. The surface wave source is given by

$$\tau_0 = E\frac{k}{2}h_0^2\rho_0 N_0 \overline{u}_0, \tag{60}$$

where h_0 is the streamline displacement at the source level and ρ_0, N_0, and $\overline{u}_0$ are also defined at the source level. The subgrid-scale orographic standard deviation σ is used to estimate h_0, with an upper bound such that the wave is not supersaturated at the source level:

$$h_0 = \min\left(2\sigma, F_c\frac{\overline{u}_0}{N_0}\right). \tag{61}$$

The source region is defined as the depth intercepted by a typical mountain within a grid box, or $0 \le z \le 2\sigma$, and τ_0 is determined at $z = 2\sigma$ so that no stress divergence takes place within the source region. The source level quantities ρ_0, N_0, u_0, v_0 are defined as mass weighted averages over the source region, with $\overline{u}_0 = (u_0^2 + v_0^2)^{1/2}$. The source quantities were all defined at the lowest model level in CCM2. The resolved wind $\overline{u}$ in (59) is obtained by projecting the local wind in the direction of the source level wind and (59) is solved in the vertical to obtain the stress profile. The stress profile is then differentiated to obtain the momentum forcing:

$$f = \frac{1}{\rho}\frac{\partial\tau}{\partial z} \ge F_c^2 E\frac{k}{2}\frac{|\overline{u}|^3}{N}\frac{1}{\rho}\frac{\partial\rho}{\partial z}, \le 0 \tag{62}$$

and f is projected back in the direction of the source wind.

The lower bound in (62) comes from the analytic solution of Lindzen (1981) and is applied to ensure that the stress divergence is of reasonable magnitude and correct sign, given the large shears that can be encountered in many of the profiles and the relatively coarse vertical resolution at which these equations are normally solved. A further condition is imposed:

$$f \ge \frac{1}{2}\frac{\overline{u}}{2\Delta t}, \tag{63}$$

which ensures that the gravity wave forcing cannot change the sign of the wind over a time step. If the bounds in (62) or (63) are applied, the stress divergence is applied in the layer below, so that the stress is still conserved in the column. This generally has the desired effect of forcing waves to break below critical levels.

There are three parameters (F_c, E, and k) appearing in (49)–(62), which must be specified. In practice, these numbers are not independent and we choose $k = 2\pi/100$ km, $F_c = 0.5$, and $E = 0.125$, which gives the same factors used in CCM2 and in McFarlane (1987).

f. Land surface model

The CCM3 incorporates version 1 of the NCAR Land Surface Model (LSM), which provides for the comprehensive treatment of land surface processes. This is a one-dimensional model of energy, momentum, water, and CO_2 exchange between the atmosphere and land, accounting for ecological differences among vegetation types, hydraulic and thermal differences among soil types, and allowing for multiple surface types including lakes and wetlands within a grid cell. LSM replaces the prescribed surface wetness, prescribed snow cover, and prescribed surface albedos in CCM2. It also replaces the land surface fluxes in CCM2, using instead flux parameterizations that include hydrological and ecological processes (e.g., soil water, phenology, stomatal physiology, and interception of water by plants).

Bonan (1996a) provides a thorough description of the model and Bonan (1996b) describes the effects of coupling the model to a version of the CCM. Bonan et al. (1997) give comparisons between simulated and observed surface fluxes for three boreal forest sites in Canada. The model has been used to study land–atmosphere exchange of CO_2 (Bonan 1995a), the sensitivity of the simulated climate to inclusion of lakes and wetlands (Bonan 1995b) and subgrid-scale runoff processes (Bonan 1996c), the effects of vegetation and soil (Kutzbach et al. 1996) and lakes and wetlands (Coe and Bonan 1997) on the African monsoon in the middle Holocene, and the effects of land use on the climate of the United States (Bonan 1998).

g. Slab ocean model

The nominal configuration of the CCM3 employs a specified distribution of sea surface temperatures, either an observed monthly mean time series or an annually repeating climatological mean. Certain applications may require a simple interactive ocean surface. The CCM3 includes a thermodynamic slab ocean model that uses specified mixed layer depths and seasonally and geographically varying ocean heat fluxes. Sea ice is calculated via a multilayer thermodynamic model. Details of this formulation and results from a control integration of the model are the subject of a future study.

3. Improvements in simulated climate

As noted, a detailed comparison of the climatology of CCM3 to observations and analyses is provided by Hurrell et al. (1998), Hack et al. (1998), and Kiehl et al. (1998). Here, we present a few key results that illustrate the differences between the CCM2 and CCM3 climates. We focus on aspects of the CCM3 that have led to a reduction in systematic errors that were identified in the simulated climate of CCM2. In particular, these biases were related to a weak Northern Hemisphere winter stationary wave pattern, a vigorous hydrologic cycle, weak zonal mean cloud radiative forcing, and excessive summertime land surface temperatures and precipitation. The results presented from the CCM2 are based on a 10-yr simulation that employs monthly

TABLE 1. Global annual average properties. Global annual mean climatological statistics from CCM2, CCM3, and observations.

	Observations	CCM2	CCM3
Outgoing longwave radiation (W m^{-2})			
all sky	234.8[a]	241.10	236.97
clear sky	264.0[a]	271.87	266.22
Absorbed solar radiation (W m^{-2})			
all sky	238.1[a]	245.35	236.88
clear sky	286.3[a]	295.49	286.42
Longwave cloud forcing (W m^{-2})	29.2[a]	30.76	29.25
Shortwave cloud forcing (W m^{-2})	−48.2[a]	−50.14	−49.54
Cloud fraction (%)			
total	52.2[b]–62.5[c]	52.86	58.83
low	26.0[c]–43.8[d]	30.52	34.75
middle	18.0[c]	22.20	20.84
high	14.0[c]	28.89	34.62
Cloud water path (mm)	0.0813[e]	—	0.0465
Precipitable water (mm)	24.7[f]	25.52	23.39
Latent heat flux (W m^{-2})	78.0[h]	104.04	89.97
Sensible heat flux (W m^{-2})	24.0[h]	9.32	20.47
Precipitation (mm day^{-1})	2.69[g]	3.58	3.09
Net surface solar radiation (W m^{-2})	168[h]	180.89	171.05
Net surface longwave radiation (W m^{-2})	66[h]	62.58	60.68
Annual mean budgets (W m^{-2})			
TOA energy budget		4.25	−0.09
SFC energy budget		4.95	−0.07
total water (P − E)		0.00	0.00

[a] ERBE.
[b] *Nimbus 7* (Hurrell and Campbell 1992).
[c] ISCCP (Rossow and Zhang 1995).
[d] Warren et al. (1988).
[e] Greenwald et al. (1995).
[f] NVAP (Randel et al. 1996).
[g] Xie and Arkin (1996).
[h] Kiehl and Trenberth (1997).

mean observed sea surface temperatures from 1979 to 1988, a so-called Atmospheric Model Intercomparison Project integration (Gates 1992; Williamson 1993). The sea surface temperatures for the 10-yr period 1979–88 used in the CCM2 simulations are identical to those employed in the CCM3 simulation. Results from the CCM3 are based on a 15-yr integration employing monthly mean observed sea surface temperatures from 1979 to 1993. Monthly climatological averages of these two simulations form the basis of the comparison. Note that differences due to length of climatological averaging time is insignificant compared to differences due to changes in model formulation.

Table 1 presents the climatological global annual mean budget results from CCM2, CCM3, and observational estimates. At the top of the atmosphere, the all sky outgoing longwave flux has decreased by 4.1 W m^{-2}, while the clear sky outgoing longwave flux has decrease by 5.7 W m^{-2} from CCM2 to CCM3. The clear sky longwave flux is now in very good agreement with the Earth Radiation Budget Experiment (ERBE) estimate of 264 W m^{-2}. This improvement in clear sky flux is due to the addition of the trace gases to CCM3. Note that most of the remaining bias of 2 W m^{-2} in clear sky flux is due to the small dry bias in CCM3 (see precipitable water values in Table 1). In the shortwave spectral region, the all sky shortwave absorbed flux at the top of the atmosphere has decreased by 8.5 W m^{-2}, while the clear sky has decreased by 9.1 W m^{-2} from CCM2 to CCM3. This large change in clear sky shortwave absorbed flux is due largely to the addition of the background aerosol in CCM3. The net radiative balance at the top of the atmosphere in CCM3 is −0.09 W m^{-2}, while it was 4.3 W m^{-2} in CCM2. This near-zero balance in CCM3 was obtained by tuning the global mean cloud cover. A near-zero top of atmosphere balance is required for coupled model studies, since any nonzero balance results in climate drift. The cloud radiative forcing values in CCM3 are in excellent agreement with the ERBE data.

The cloud fraction in CCM3 is 6% larger than CCM2. The CCM3 cloud fraction of 59% is closer to the latest observational estimates of 63%. The largest increase in cloud cover occurs for upper-tropospheric cloud, which is a direct result of the new deep convection scheme's tendency to moisten the upper troposphere. An indication of the reduction in the vigorous nature of the CCM2 hydrologic cycle is the 14 W m^{-2} decrease in latent heat flux from CCM2 to CCM3. This is a significant change in the CCM simulation toward observational estimates. Of course this change in global mean latent heat flux must be balanced by accompanying

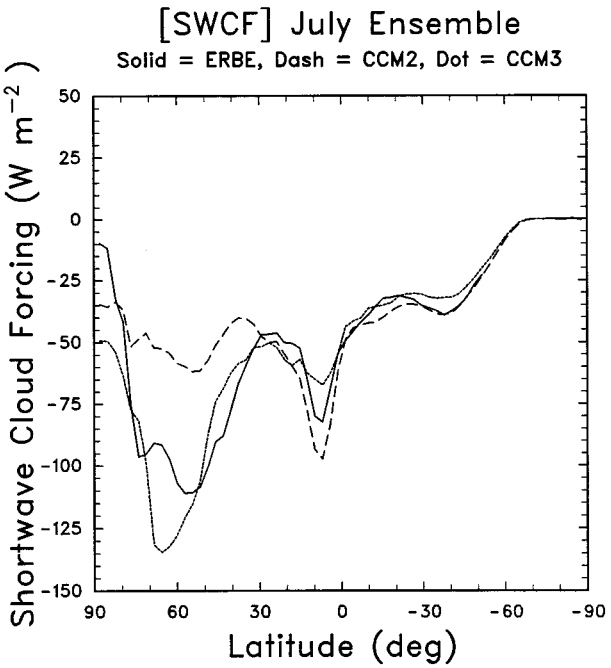

FIG. 1. The ensemble July mean zonal-mean SWCF (W m^{-2}) for the CCM2 (– – –), CCM3 (·····), and ERBE (——).

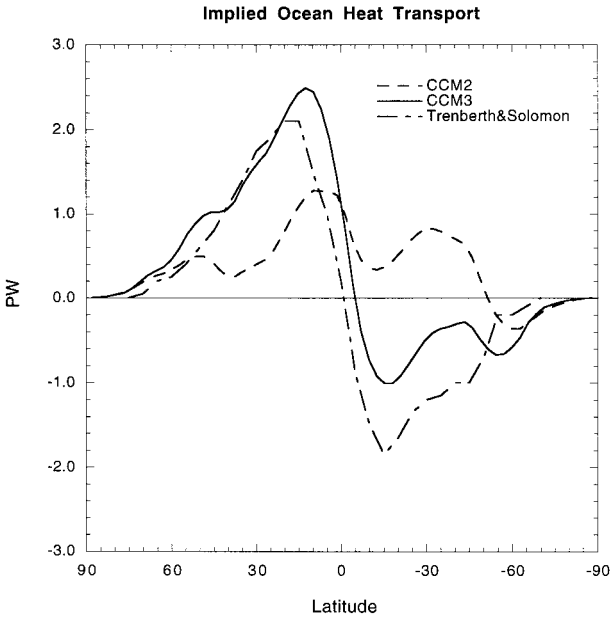

FIG. 2. The implied ocean heat transport (PW) from CCM2 (– – –), CCM3 (——), and the observational estimate of Trenberth and Solomon (1994) (– – –).

changes in the other surface energy fluxes. The largest of these changes is the sensible heat flux, which has increased by 11 W m^{-2}. Note that it is difficult to directly compare these changes, since the net CCM2 surface flux was out of balance by nearly 5 W m^{-2}.

As pointed out in Kiehl et al. (1994) the shortwave cloud forcing (SWCF) in CCM2 exhibited a very weak cloud forcing in storm track regions. This large local bias (~50 W m^{-2}) in zonal-mean SWCF has important implications for calculating the implied meridional ocean heat transport from an atmospheric model (see Gleckler et al. 1995). Figure 1 shows the zonal-mean SWCF for July from CCM3, CCM2, and the ERBE data. The ERBE data show significant SWCF centered at 60° north (~−115 W m^{-2}). The CCM2 cloud forcing is far too weak in this region, while the CCM3 shortwave forcing is slightly too large. This is a significant improvement in this field. Hack (1997a) has shown the major source of the improved extratropical SWCF in CCM3 is due to a combination of the diagnostic cloud water paramaterization and the particle size parameterization. As Gleckler et al. (1995) indicate, an accurate simulation of this field is a necessary condition for an accurate simulation of the implied ocean heat transport deduced from an atmospheric climate model. Figure 2 shows the implied ocean heat transport from CCM2, CCM3, and the observational estimate of Trenberth and Solomon (1994). The implied ocean heat transport is obtained from the net surface energy flux produced by the atmospheric model. This figure indicates that CCM2 had a very weak implied ocean transport, with the incorrect sign of transport in the Southern Hemisphere (i.e., equatorward). CCM3 has the correct sign of transport (i.e., poleward) in the Southern Hemisphere, and the magnitude is vastly improved over that of CCM2. This improvement is, in part, due to the improved simulation of SWCF. However, although the proper simulation of shortwave radiative effects of clouds is a necessary condition for realistic meridional oceanic heat transport, it is not sufficient. The principal reason for this remarkable change is the introduction of the Zhang and McFarlane (1995) deep cumulus convection scheme. The deep convection parameterization produces a sharp reduction in equatorial surface latent heat fluxes, thus increasing the poleward heat transport requirement for the ocean circulation (see Hack 1998b).

Figure 3 shows the zonal-mean annual clear sky outgoing longwave flux at the top of the atmosphere from CCM3 and CCM2. The addition of the trace gases has led to a substantial reduction in clear sky outgoing longwave flux. In the Tropics the clear sky flux has decreased by ~12 W m^{-2}. As seen in Table 1, the CCM3 clear sky flux is much closer to the ERBE observations than the value from the CCM2.

Figure 4 presents the zonal-mean annual mean surface latent heat flux from CCM2 and CCM3. As mentioned earlier, the CCM2 had an overly vigorous hydrologic cycle. One signature of this is the magnitude of the latent heat flux. In the Tropics the latent heat flux has decreased by ~40 W m^{-2}. This dramatic reduction in surface latent heat flux has brought the CCM3 much closer to the NCAR Ocean Model data (Doney et al. 1998). Roughly a third of this decrease in the Tropics

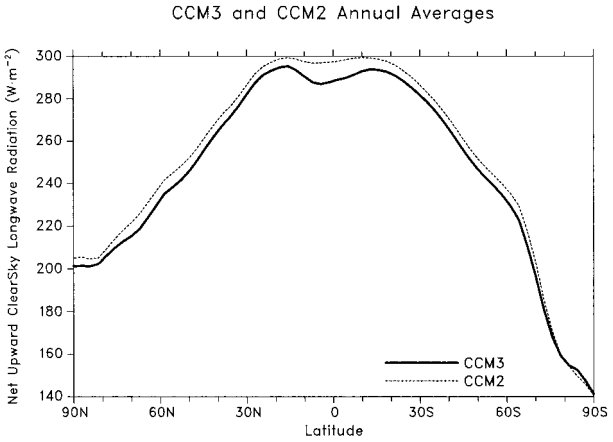

FIG. 3. The zonal-mean ensemble annual mean clear sky outgoing longwave flux (W m^{-2}) from CCM2 (– – –) and CCM3 (———).

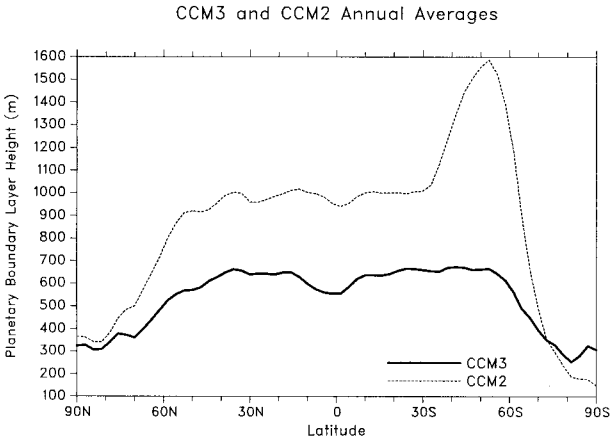

FIG. 5. The zonal-mean ensemble annual mean planetary boundary layer height (m) from CCM2 (– – –) and CCM3 (———).

is due to changes in boundary layer formulation and the remaining two-thirds is due to the new deep convection scheme. Another measure of the change in boundary layer properties is the boundary layer height (Fig. 5). The new formulation in CCM3 has reduced the height of the boundary layer by ~400 m at most latitudes, with a larger reduction in the Southern Hemisphere storm track region. Again, this reduction in boundary layer height from CCM2 to CCM3 is an improvement to the model climatology. Another indication of the reduction in the strength of the hydrologic cycle between CCM3 and CCM2 is seen in the zonal-mean precipitation (Fig. 6). There is a uniform reduction in precipitation at almost all latitudes of almost 1 mm day^{-1}; that is, the magnitude of extratropical reductions in precipitation are comparable to precipitation changes in the ITCZ. Although the ITCZ precipitation maximum is only modestly reduced and shifted toward the equator, the seasonal zonal averages show considerably greater differences between the CCM2 and CCM3 (Hack et al. 1998). The seasonal maxima in ITCZ precipitation are substantially reduced and are much more consistent with with recent observational estimates (e.g., Xie and Arkin 1996).

Hack et al. (1994) noted that a significant bias existed in the Northern Hemisphere winter stationary wave pattern simulated by CCM2. Figure 7 shows the 500-mb height field from CCM3 and CCM2 for December–February (DJF) seasonal average. The position and strength of the North Pacific ridge is greatly improved over that of CCM2. The improvement in this ridge structure is due to improvements in cloud optical properties (see Kiehl 1994; Hack 1998a) and to shifts in tropical heating associated with the new deep convective scheme of Zhang and McFarlane (1995). Another measure of this improved dynamical structure is shown in Fig. 8, which shows the difference in 200-mb perturbation streamfunction between CCM3 and NCEP reanalysis, and CCM2 and NCEP reanalysis. Biases in the CCM3 perturbation streamfunction are very small, with near-exact agreement with the reanalysis. For CCM2, however,

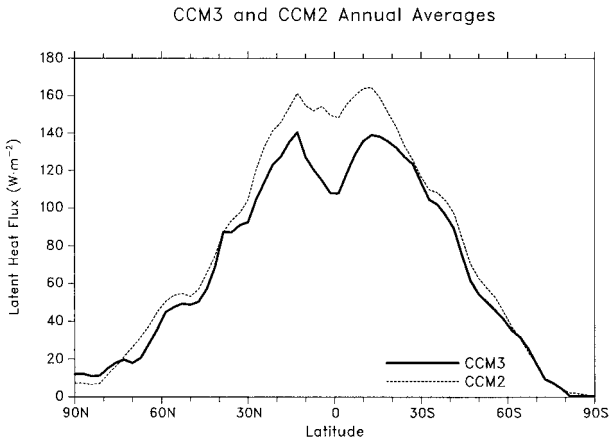

FIG. 4. The zonal-mean ensemble annual mean surface latent heat flux (W m^{-2}) from CCM2 (– – –) and CCM3 (———).

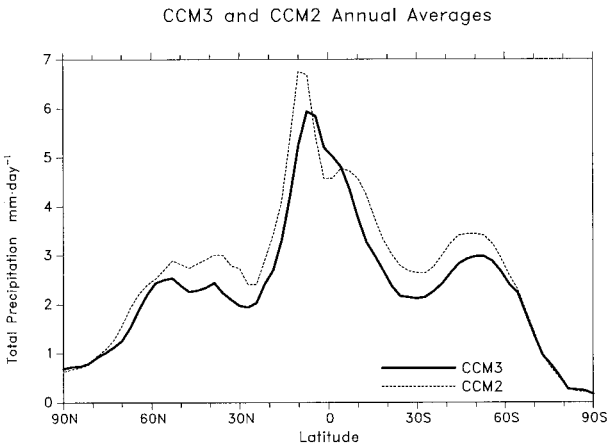

FIG. 6. The zonal-mean ensemble annual mean precipitation rate (mm day^{-1}) from CCM2 (– – –) and CCM3 (———).

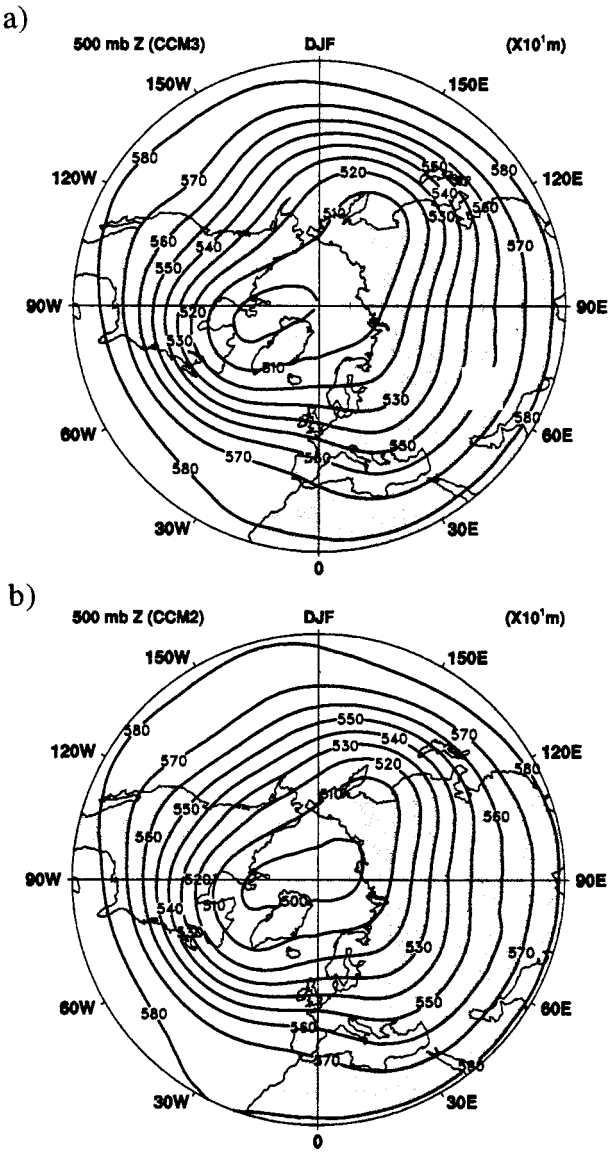

FIG. 7. The ensemble mean DJF seasonal mean of Northern Hemisphere 500-mb height (×10 m) from (a) CCM3 and (b) CCM2.

there is a notable bias with a reverse Pacific–North American pattern. The anomalously large bias in the North Pacific, centered along the date line, is an indication of the phase shift in the Pacific ridge structure noted by Hack et al. (1994). A final measure of the improvement in the dynamical simulation of the CCM is shown in the 200-mb zonal wind component (Fig. 9). Figure 9 shows the difference in the 200-mb zonal wind between CCM3 and the NCEP reanalysis for an ensemble DJF seasonal mean. For CCM3, the large bias in 200-mb zonal wind is in the Southern Hemisphere located south of Australia. There are large biases (>10 m s^{-1}) in CCM2, especially in the tropical and North Pacific Ocean regions.

The largest biases over land in CCM2 occured in the Northern Hemisphere summer [see plate 1b of Hack et al. (1994)], where the model-simulated surface temperature was too warm by as much as 8°–10°. Figure 10 shows the difference in surface air temperature between CCM3 and CCM2 for DJF and JJA seasonal averages. In JJA, the CCM3 surface air temperatures have decreased by as much as 10° over large regions of the Northern Hemisphere continents. This reduction is due to the implementation of the LSM and changes to the cloud optical properties (Kiehl 1994; Hack 1998a). Changes in surface temperatures in Southern Hemisphere summer also help alleviate biases that existed in CCM2. Another, significant bias over land in CCM2 was an overprediction of precipitation [see Fig. 20 in Hack et al. (1994)]. Figure 11 shows the change in precipitation over land between CCM3 and CCM2 for DJF and JJA seasonal averages. There are significant (>16 mm day^{-1}) decreases in precipitation over tropical land regions. In particular, the precipitation over Brazil has decreased in DJF. These reductions are mainly associated with changes to cloud optics and the addition of the LSM.

Finally, to give an overall indication of how the simulated climate of four generations of the CCM has improved, we consider the following global metric. Figure 12 shows the normalized mean square error (NMSE) skill score (tripartite wide bar) and a complementary control statistic, scaled variance ratio (narrow bar), for the January average 200-mb height field in the Northern Hemisphere for the various versions of the NCAR CCM, which have been frozen over the last 15 yr. This score, discussed in Williamson (1995), is defined by

$$\mathrm{NMSE}\ (z_m) = \overline{(z_m - z_a)^2}/\overline{(z_a')^2}, \tag{64}$$

where the overbar denotes the average from 30°N to the pole, the prime denotes the deviation from that average, and the subscripts m and a denote the model (CCM) and analyses [European Centre for Medium-Range Weather Forecasts (ECMWF)], respectively. The normalized mean square error is plotted in Fig. 12 as three additive components:

$$\mathrm{NMSE}(z_m) = \left(\frac{\overline{z_m} - \overline{z_a}}{s_a}\right)^2 + \left(r_{ma} - \frac{s_m}{s_a}\right)^2 + (1 - r_{ma}^2), \tag{65}$$

each of which is nonnegative. The variances are denoted by s_m^2 and s_a^2 and the correlation by r_{ma}. The first component is the unconditional bias, indicated by hatching in the figure, the second is the conditional bias, indicated by the solid fill, and the third is the lack of correlation, indicated by the open component.

The unconditional bias vanishes only when the mean error is zero. The conditional bias includes both amplitude and phase errors, and is conditional in the sense of dependency on the atmospheric state so that, for example, in the case of no phase errors or perfect correlations ($r_{ma} = 1$), where the atmosphere is low, the model

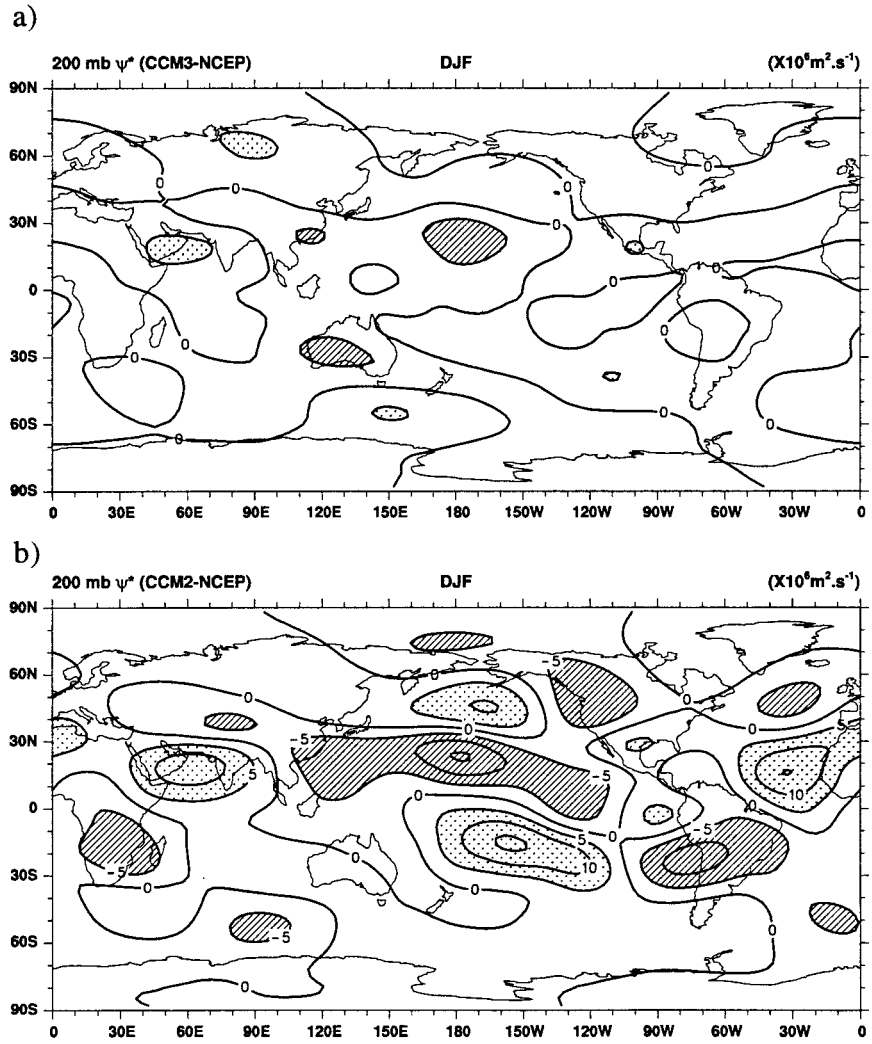

FIG. 8. The ensemble mean DJF seasonal mean difference of model 200-mb perturbation streamfunction ($\times 10^6$ m^2 s^{-1}) against NCEP reanalysis for (a) CCM3 and (b) CCM2.

is lower, and where the atmosphere is high, the model is higher, etc. The third term measures the lack of correlation and is due to phase errors.

The narrow bars on the left of each NMSE tripartite bar are the scaled variance ratio (SVR), which serves as a control score for the NMSE:

$$\mathrm{SVR}(z_m) = \left(\frac{S_m}{S_a}\right)^2 \mathrm{NMSE}(z_m). \tag{66}$$

It indicates whether the model variance is greater than or less than that of the atmosphere, and thus, how it might be affecting the conditional bias.

The scores are calculated for the resolutions at which the models were developed (R15 for CCM0 and CCM1, and T42 for CCM2 and CCM3) compared to the ECMWF analyses as archived at NCAR (Trenberth 1992) averaged from 1979 through 1988. The simulated climate has clearly improved with each succeeding version, primarily in a reduction of the unconditional bias up to CCM2 and as a reduction of the lack of correlation with CCM3. The reduction of the unconditional bias was in fact a design goal in the development of CCM2. The component associated with the correlation, however, was not improved in a succeeding version up to CCM2, and, in fact, became slightly larger in CCM2, as noted by Hoerling et al. (1993) and Hack et al. (1994). One of the design goals for CCM3 was the reduction of the correlation error. As seen in Fig. 12, this was largely successful. The most significant component of the error remaining in CCM3 is the unconditional bias, and is a reflection of the 1°–2° zonal average temperature error throughout the winter extratropical troposphere in the simulation.

Concerning the control statistic, SVR, CCM0, CCM2, and CCM3 all have larger variance than the atmosphere, whereas CCM1 has less. The larger model variances are probably contributing to the conditional biases. How-

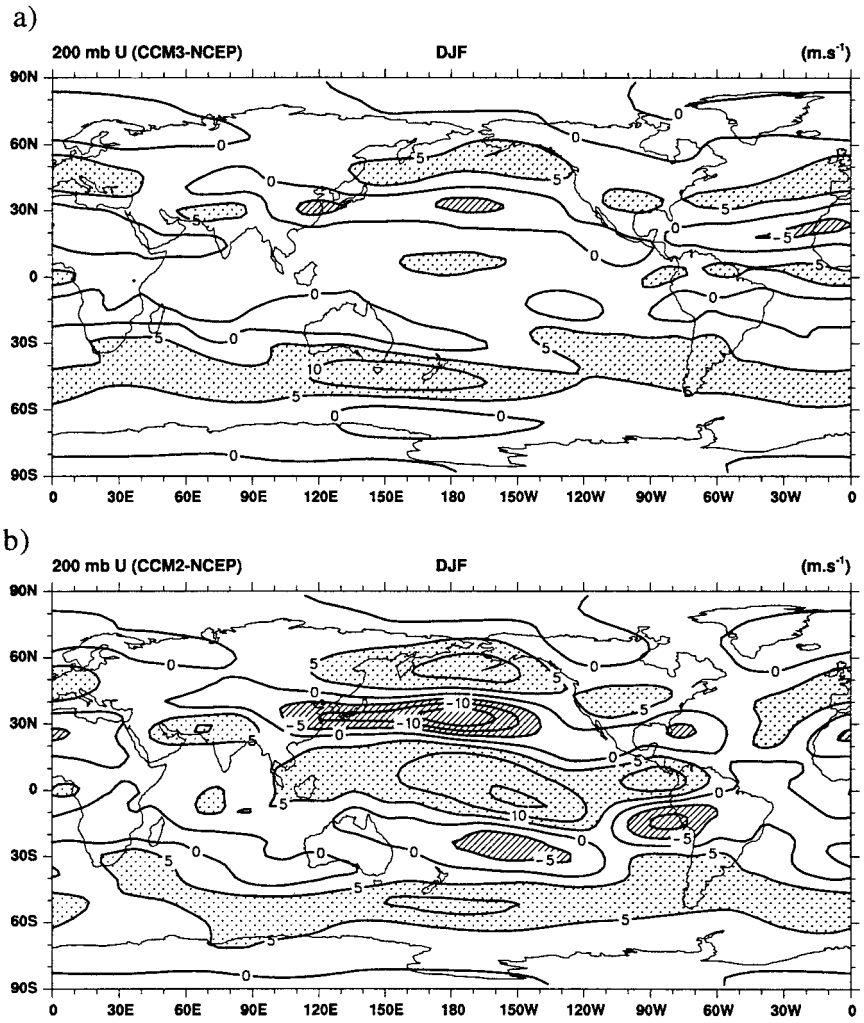

FIG. 9. The ensemble mean DJF seasonal mean difference of model 200-mb zonal wind component (m s^{-1}) against NCEP reanalysis for (a) CCM3 and (b) CCM2.

ever, for CCM3, the SVR is close enough to the NMSE to indicate that the NMSE is not artificially low due to damping of the model height field.

4. Summary

The new physical and dynamical formulations in CCM3 have been described. The improvements to the physical processes include new cloud properties, a new deep convection parameterization, a reformulation of the surface and boundary layer processes, the inclusion of trace gas radiative properties, and the addition of a new land surface model. The development and implementation of these processes was motivated by biases in the simulated climate of the CCM2. It is important to note that many of these separate processes interact with one another in subtle and nonlinear ways. These interactions, which exist in nature, emphasize the importance of an integrated approach to climate model development.

The new parameterizations have had a major impact on the simulated climate of the CCM. The changes in cloud parameterization, in particular the cloud microphysics properties, have a significant impact on both the radiative and dynamical simulation of the CCM3 (see, e.g., Hack 1998a; Kiehl 1994). In particular, the generalization of cloud water content and cloud particle size shift the diabatic heating in the Tropics, which has a beneficial impact on the simulation of the Northern Hemisphere winter stationary wave pattern. The improved stationary wave pattern leads, in turn, to an improved zonal wind structure.

Changes in boundary layer parameterization and the inclusion of the new deep convection scheme have also led to major improvements in the simulation of the dynamical and hydrologic cycle of the CCM. These new processes result in a weaker hydrologic cycle in CCM3 compared to that in the CCM2, which was too strong. The surface latent heat flux is significantly reduced, especially in the Tropics. Associated with the reduction

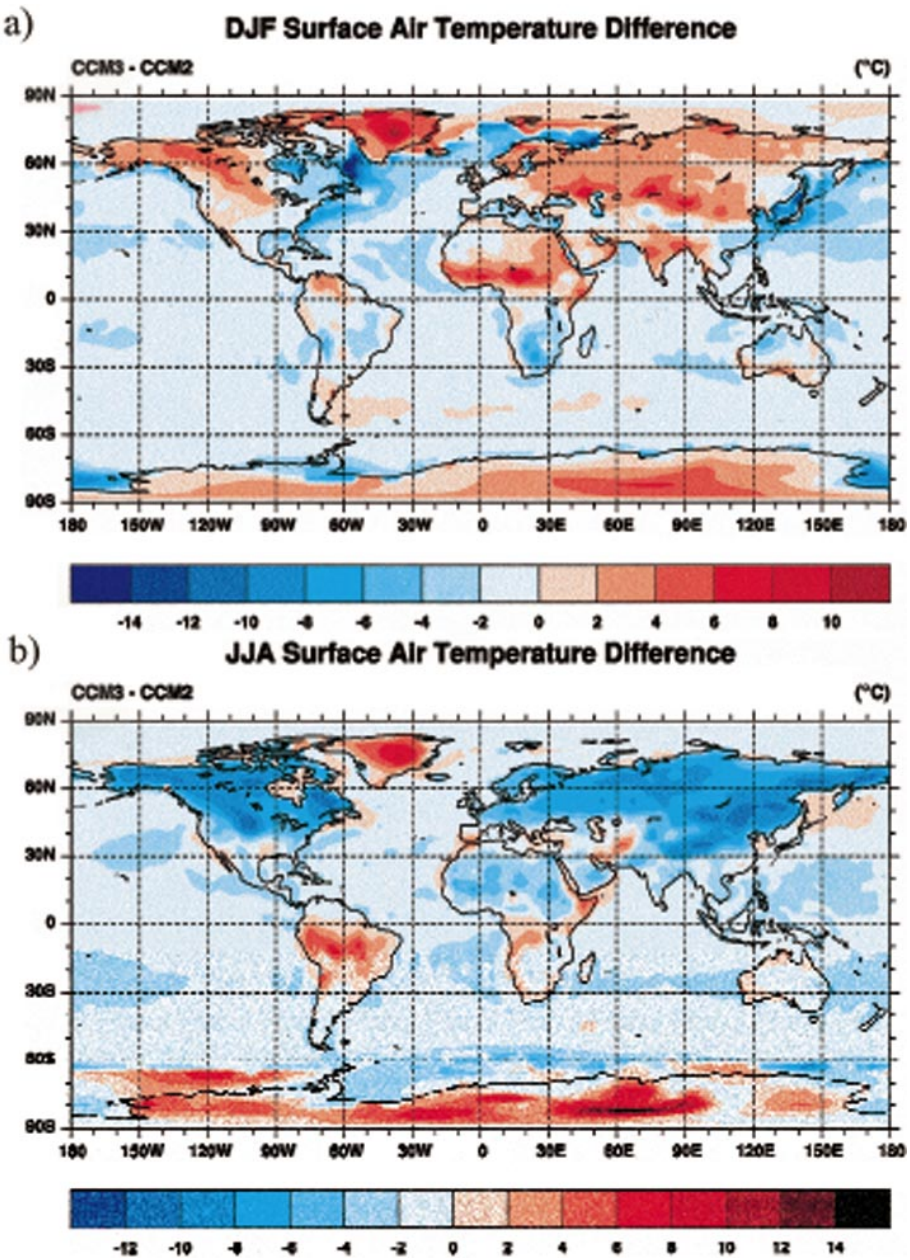

FIG. 10. Difference in surface air temperature (C) between CCM3 and CCM2 for ensemble (a) DJF seasonal mean and (b) June–July–August (JJA) seasonal mean.

in latent heat is a reduced precipitation rate at all latitudes. Again, these changes are significant improvements to the simulated climate, when compared to recent satellite and surface estimates of the hydrologic cycle [see Hack et al. (1998) for details]. Over land, large precipitation reductions (>15 mm day^{-1}) in CCM3 have improved the regional hydrologic processes. These reductions are due to the changes in cloud optics (Kiehl 1994; Hack 1998a), changes in the treatment of land surface processes, and to changes in convection. For example, the CCM3 provides an excellent simulation of the Indian monsoon (see Hack et al. 1998).

Improvements in the top of atmosphere and surface energy fluxes in CCM3 have resulted in a significant improvement in the simulation of the implied ocean heat transport. The implied ocean heat transport from CCM3 is in excellent agreement with the explicit ocean heat transport from the uncoupled NCAR ocean model (see Kiehl et al. 1998). This agreement is one reason that the CSM climate is so stable (Boville and Gent 1998).

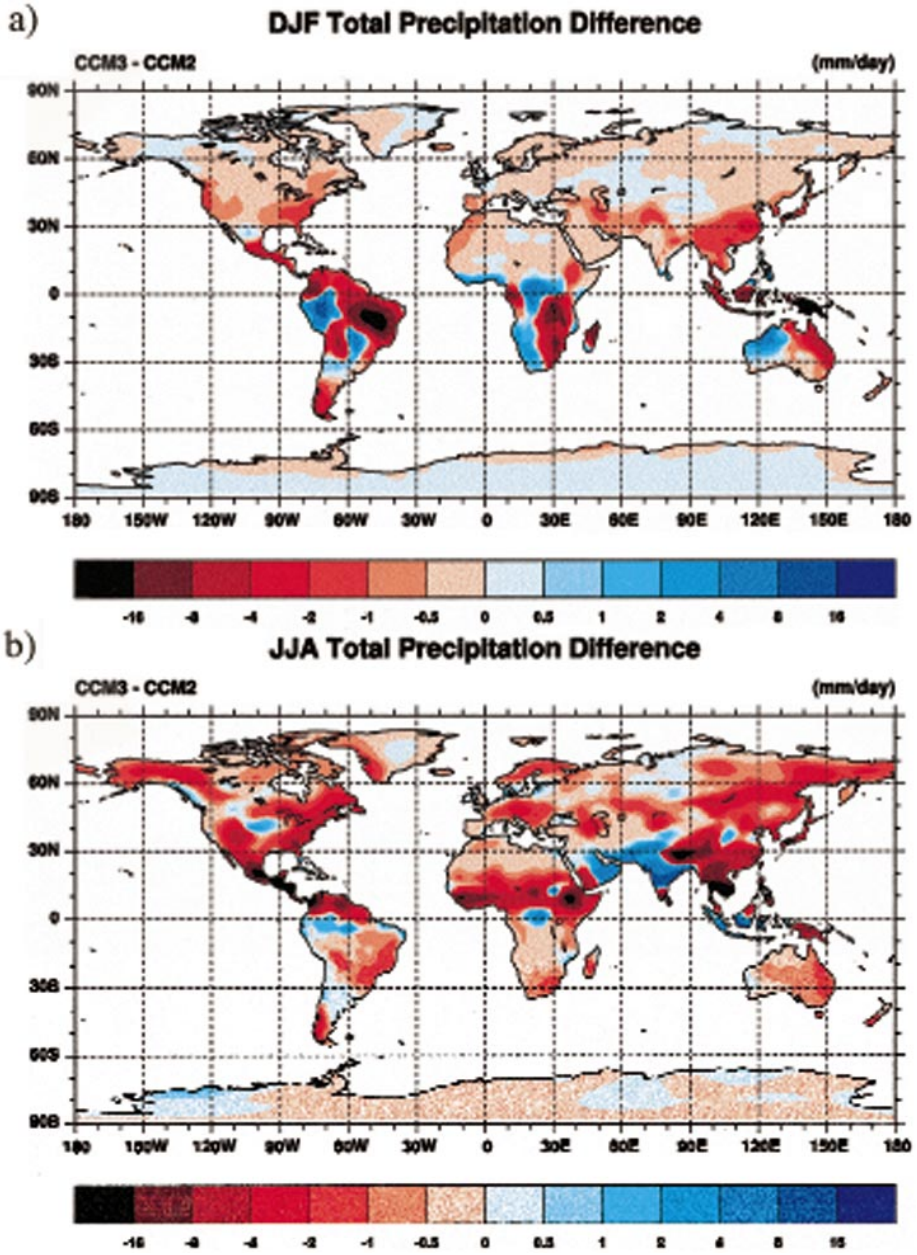

FIG. 11. Difference in precipitation over land (mm day^{-1}) between CCM3 and CCM2 for ensemble (a) DJF seasonal mean and (b) JJA seasonal mean.

As the history of the Community Climate Model indicates, the model will continue to evolve. The direction of the evolution of the model will be motivated by further improving the simulated climate, and generalization of parameterizations to include other aspects of the climate system. For example, development of a semi-Lagrangian dynamical formulation of CCM3 has been completed (Williamson et al. 1998). This formalism allows for increased horizontal resolution with minimal computational burden. Increased vertical resolution will also be a part of future versions of the CCM. A prognostic cloud water scheme has also been implemented into CCM3 (Rasch and Kristjansson 1998). This generalization of CCM3 allows for the inclusion of cloud chemistry interactions. Implementation of aerosol models within the CCM3 is also under way. This will allow for a more realistic treatment of atmospheric aerosols and their effects on climate. Future improvements in convective parameterizations are also required to reduce biases in the position of convection and the impact of this process on the vertical distribution of moisture. Thus, there is commitment in the NCAR Climate Mod-

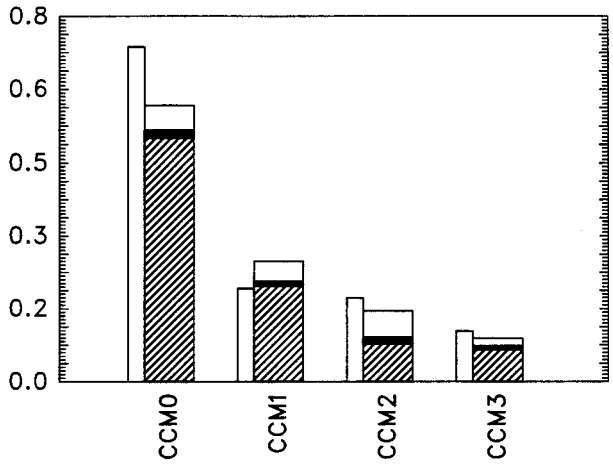

FIG. 12. Wide, tripartite bars: NMSE skill score for the January average 200-mb height field in the Northern Hemisphere for CCM0, CCM1, CCM2, and CCM3; unconditional bias—hatched, conditional bias—solid, and lack of correlation—open. Narrow single sidebars: SVR control score.

eling Section to continually provide improved versions of the CCM to the climate community.

Acknowledgments. We thank the following members of the Climate Modeling Section for their tremendous contribution to the development of the CCM3: T. Acker, J. Rosinski, J. Olson, J. Truesdale, and M. Vertenstein. We especially thank B. Briegleb for his development of the slab ocean model and aerosol components to CCM3. We thank J. Hurrell for numerous conversations on the analysis of the CCM. We would like to thank our collaborators A. Holtslag (Utrecht University) and G. Zhang (Scripps Institution of Oceanography) for their contributions to the development of CCM3. We also thank J. Dunn for help with some of the figures. Finally, we wish to thank P. Fisher for her help with the preparation of this manuscript.

REFERENCES

Acker, T. L., L. E. Buja, J. M. Rosinski, and J. E. Truesdale, 1996: Users' guide to NCAR CCM3. NCAR Tech. Note NCAR/TN-421+IA, 210 pp. [Available from National Center for Atmospheric Research, Boulder, CO 80307.]

Anthes, R. A., 1986: Summary of workshop on the NCAR community climate/forecast models, 14–26 July 1985, Boulder, Colorado. *Bull. Amer. Meteor. Soc.,* **67,** 94–198.

Bonan, G. B., 1995a: Land–atmosphere CO_2 exchange simulated by a land surface process model coupled to an atmospheric general circulation model. *J. Geophys. Res.,* **100,** 2817–2831.

——, 1995b: Sensitivity of a GCM simulation to inclusion of inland water surfaces. *J. Climate,* **8,** 2691–2704.

——, 1996a: A land surface model (LSM version 1.0) for ecological, hydrological, and atmospheric studies: Technical description and user's guide. NCAR Tech. Note NCAR/TN-417+STR, 150 pp. [Available from National Center for Atmospheric Research, Boulder, CO 80307.]

——, 1996b: The NCAR land surface model (LSM version 1.0) coupled to the NCAR Community Climate Model. NCAR Tech. Note NCAR/TN-429+STR, 171 pp. [Available from National Center for Atmospheric Research, Boulder, CO 80307.]

——, 1996c: Sensitivity of a GCM simulation to subgrid infiltration and surface runoff. *Climate Dyn.,* **12,** 279–285.

——, 1997: Effects of land use on the climate of the United States. *Climate Change,* **37,** 449–486.

——, 1998: The land surface climatology of the NCAR Land Surface Model (LSM 1.0) coupled to the NCAR Community Climate Model (CCM3). *J. Climate,* **11,** 1307–1326.

——, K. J. Davis, D. Baldocchi, D. Fitzjarrald, and H. Neumann, 1997: Comparison of the NCAR LSM1 land surface model with BOREAS aspen and jack pine tower fluxes. *J. Geophys. Res.,* **102,** 29 065–29 075.

Boville, B. A., and P. R. Gent, 1998: The NCAR Climate System Model, version one. *J. Climate,* **11,** 1115–1130.

Briegleb, B. P., 1992: Delta-Eddington approximation for solar radiation in the NCAR Community Climate Model. *J. Geophys. Res.,* **97,** 7603–7612.

Cess, R. D., 1985: Nuclear war: Illustrative effects of atmospheric smoke and dust upon solar radiation. *Climate Change,* **7,** 237–251.

Coe, M. T., and G. B. Bonan, 1997: Feedbacks between climate and surface water in northern Africa during the middle Holocene. *J. Geophys. Res.,* **102,** 11 087–11 101.

Dandin, P., C. Pontikis, and E. Hicks, 1997: Sensitvity of a GCM to changes in the droplet effective radius parameterization. *Geophys. Res. Lett.,* **24,** 437–440.

Deardorff, J. W., 1972: Parameterization of the planetary boundary layer for use in general circulation models. *Mon. Wea. Rev.,* **100,** 93–106.

Doney, S. C., W. G. Large, and F. O. Bryan, 1998: Surface ocean fluxes and water-mass transformation rates in the coupled NCAR Climate System Model. *J. Climate,* **11,** 1420–1441.

Duynkerke, P. G., 1988: Application of the $E - \epsilon$ turbulence closure model to the neutral and stable atmospheric boundary layer. *J. Atmos. Sci.,* **45,** 865–880.

Ebert, E. E., and J. A. Curry, 1992: A parameterization of ice cloud optical properties for climate models. *J. Geophys. Res.,* **97,** 3831–3836.

Gates, W. L., 1992: AMIP: The Atmospheric Model Intercomparison Project. *Bull. Amer. Meteor. Soc.,* **73,** 1962–1970.

Geleyn, J. F., 1988: Interpolation of wind, temperature and humidity values from model levels to the height of measurement. *Tellus,* **40A,** 347–351.

Gleckler, P. J., and Coauthors, 1995: Cloud-radiative effects on implied oceanic energy transport as simulated by atmospheric general circulation models. *Geophys. Res. Lett.,* **22,** 791–794.

Greenwald, T. J., G. L. Stephens, S. A. Christopher, and T. H. Vonder Haar, 1995: Observations of the global characteristics and regional radiative effects of marine cloud liquid water. *J. Climate,* **8,** 2928–2946.

Hack, J. J., 1994: Parameterization of moist convection in the National Center for Atmospheric Research Community Climate Model (CCM2). *J. Geophys. Res.,* **99,** 5551–5568.

——, 1998a: Sensitivity of the simulated climate to a diagnostic formulation for cloud liquid water. *J. Climate,* in press.

——, 1998b: An analysis of the improvement in implied meridional ocean energy transport as simulated by the NCAR CCM3. *J. Climate,* **11,** 1237–1244.

——, B. A. Boville, B. P. Briegleb, J. T. Kiehl, P. J. Rasch, and D. L. Williamson, 1993: Description of the NCAR Community Climate Model (CCM2). NCAR Tech. Note NCAR/TN-382+STR, 108 pp. [Available from National Center for Atmospheric Research, Boulder, CO 80307.]

——, ——, J. T. Kiehl, P. J. Rasch, and D. L. Williamson, 1994: Climate statistics from the NCAR Community Climate Model (CCM2). *J. Geophys. Res.,* **99,** 20 785–20 813.

——, J. T. Kiehl, and J. W. Hurrell, 1998: The hydrologic and thermodynamic characteristics of the NCAR CCM3. *J. Climate,* **11,** 1179–1206.

Hoerling, M. P., L. L. DeHaan, and J. W. Hurrell, 1993: Diagnosis and sensitivity of the 200 hPa circulation in the NCAR Community Climate Models. NCAR/TN-394+STR, 68 pp. [Available from National Center for Atmospheric Research, Boulder, CO 80307.]

Holtslag, A. A. M., and B. A. Boville, 1993: Local versus nonlocal boundary-layer diffusion in a global climate model. *J. Climate,* **6,** 1825–1842.

Hurrell, J. W., and G. G. Campbell, 1992: Monthly mean global satellite data sets available in CCM history tape format. NCAR Tech. Note NCAR/TN-371+STR, 94 pp. [Available from National Center for Atmospheric Research, Boulder, CO 80307.]

——, J. J. Hack, B. A. Boville, D. L. Williamson, and J. T. Kiehl, 1998: The dynamical simulation of the NCAR Community Climate Model version 3 (CCM3). *J. Climate,* **11,** 1207–1236.

Kiehl, J. T., 1994: Sensitivity of a GCM climate simulation to differences in continental versus maritime cloud drop size. *J. Geophys. Res.,* **99,** 23 107–23 115.

——, and V. Ramanathan, 1983: CO_2 radiative parameterization used in climate models: Comparison with narrow band models and with laboratory data. *J. Geophys. Res.,* **88,** 5191–5202.

——, and B. P. Briegleb, 1991: A new parameterization of the absorptance due to the 15 μm band system of carbon dioxide. *J. Geophys. Res.,* **96,** 9013–9019.

——, and ——, 1993: The relative roles of sulfate aerosols and greenhouse gases in climate forcing. *Science,* **260,** 311–314.

——, and K. E. Trenberth, 1997: Earth's annual global mean energy budget. *Bull. Amer. Meteor. Soc.,* **78,** 197–208.

——, J. J. Hack, and B. P. Briegleb, 1994: The simulated earth radiation budget of the NCAR CCM2 and comparisons with the Earth Radiation Budget Experiment (ERBE). *J. Geophys. Res.,* **99,** 20 815–20 827.

——, ——, G. B. Bonan, B. A. Boville, B. P. Briegleb, D. L. Williamson, and P. J. Rasch, 1996: Description of the NCAR Community Climate Model (CCM3). NCAR Tech. Note, NCAR/TN-420+STR, 152 pp. [Available from National Center for Atmospheric Research, Boulder, CO 80307.]

——, ——, and J. W. Hurrell, 1998: The energy budget of the NCAR Community Climate Model: CCM3. *J. Climate.,* **11,** 1151–1178.

Kutzbach, J., G. Bonan, J. Foley, and S. P. Harrison, 1996: Vegetation and soil feedbacks on the response of the African monsoon to orbital forcing in the early to middle Holocene. *Nature,* **384,** 623–626.

Large, W. G., and S. Pond, 1982: Sensible and latent head flux measurements over the ocean. *J. Phys. Oceanogr.,* **12,** 464–482.

——, J. C. McWilliams, and S. C. Doney, 1994: Oceanic vertical mixing: A review and a model with a nonlocal boundary layer parameterizatin. *Rev. Geophys.,* **32,** 363–403.

Lindzen, R. S., 1981: Turbulence and stress swing to gravity wave and tidal breakdown. *J. Geophys. Res.,* **86,** 9707–9714.

Liou, K. N., 1992: *Radiation and Cloud Processes in the Atmosphere.* Oxford University Press, 487 pp.

McFarlane, N. A., 1987: The effect of orographically excited wave drag on the general circulation of the lower stratosphere and troposphere. *J. Atmos. Sci.,* **44,** 1775–1800.

Moeng, C.-H., and P. P. Sullivan, 1994: A comparison of shear- and bouyancy-driven planetary boundary layer flows. *J. Atmos. Sci.,* **51,** 999–1022.

Pitcher, E. J., R. C. Malone, V. Ramanathan, M. L. Blackmon, K. Puri, and W. Bourke, 1983: January and July simulations with a spectral general circulation model. *J. Atmos. Sci.,* **40,** 580–604.

Ramanathan, V., 1976: Radiative transfer within the earth's troposphere and stratosphere: A simplified radiative-convective model. *J. Atmos. Sci.,* **33,** 1330–1346.

——, and P. Downey, 1986: A nonisothermal emissivity and absorptivity formulation for water vapor. *J. Geophys. Res.,* **91,** 8649–8666.

——, R. J. Cicerone, H. B. Singh, and J. T. Kiehl, 1985: Trace gas trends and their potential role in climate change. *J. Geophys. Res.,* **90,** 5547–5566.

Randel, D. L., T. H. Vonder Haar, M. A. Ringerud, G. L. Stephens, T. J. Greenwald, and C. L. Combs, 1996: A new global water vapor dataset. *Bull. Amer. Meteor. Soc.,* **77,** 1233–1246.

Rasch, P. J., and J. E. Kristjánsson, 1998: A comparison of the CCM3 model climate using diagnosed and predicted condensate parameterizations. *J. Climate,* in press.

Rogers, R. R., and M. K. Yau, 1989: *A Short Course in Cloud Physics.* Pergamon Press, 293 pp.

Rossow, W. B., and Y.-C. Zhang, 1995: Calculation of surface and top of atmosphere radiative fluxes from physical quantities based on ISCCP data sets. Part II: Validation and first results. *J. Geophys. Res.,* **100,** 1167–1197.

Slingo, J. M., 1987: The development and verification of a cloud prediction scheme for the ECMWF model. *Quart. J. Roy. Meteor. Soc.,* **113,** 899–927.

——, 1989: A GCM parameterization for the shortwave radiative properties of water clouds. *J. Atmos. Sci.,* **46,** 1419–1427.

Stephens, G. L., 1984: The parameterization of radiation for numerical weather prediction and climate models. *Mon. Wea. Rev.,* **112,** 826–867.

Trenberth, K. E., 1992: Global analyses from ECMWF and atlas of 1000 to 10 mb circulation statistics. NCAR Tech. Note NCAR/TN-373+STR, 191 pp. [Available from National Center for Atmospheric Research, Boulder, CO 80307.]

——, and A. Solomon, 1994: The global heat balance: Heat transports in the atmosphere and ocean. *Climate Dyn.,* **10,** 107–134.

Vogelezang, D. H. P., and A. A. M. Holtslag, 1996: Evaluation and model impacts of alternative boundary-layer height formulations. *Bound.-Layer Meteor.,* **81,** 245–269.

Warren, S. G., C. J. Hahn, J. London, R. M. Chervin, and R. L. Jenne, 1988: Global distribution of total cloud cover and cloud type amounts over the ocean. NCAR Tech. Note NCAR/TN-317+STR, 107 pp. [Available from National Center for Atmospheric Research, Boulder, CO 80307.]

Williamson, D. L., 1983: Description of NCAR Community Climate Model (CCM0B). NCAR Tech. Note NCAR/TN-210+STR, 88 pp. [Available from National Center for Atmospheric Research, Boulder, CO 80307.]

——, 1993: CCM2 datasets and circulation statistics. NCAR Tech. Note NCAR/TN-391+STR, 85 pp. [Available from National Center for Atmospheric Research, Boulder, CO 80307.]

——, 1995: Skill scores from the AMIP Simulations. *Proc. AMIP Scientific Conf.,* Monterey, CA, World Climate Research Program, 253–258.

——, and J. G. Olson, 1994: Climate simulations with a semi-Lagrangian version of the NCAR Community Climate Model. *Mon. Wea. Rev.,* **122,** 1594–1610.

——, ——, and B. A. Boville, 1998: A comparison of semi-Lagrangian and Eulerian tropical climate simulations. *Mon. Wea. Rev.,* **126,** 1001–1012.

Xie, P., and P. A. Arkin, 1996: Analyses of global monthly precipitation using guage observations, satellite estimates, and numerical model predictions. *J. Climate,* **9,** 840–858.

Xu, K.-M., and S. K. Krueger, 1991: Evaluation of cloud models using a cumulus ensemble model. *Mon. Wea. Rev.,* **119,** 342–367.

Zender, C. S., and J. T. Kiehl, 1997: Sensitivity of climate simulations to radiative effects of tropical anvil structure. *J. Geophys. Res.,* **102,** 23 793–23 803.

Zhang, G. J., and N. A. McFarlane, 1995: Sensitivity of climate simulations to the parameterization of cumulus convection in the Canadian Climate Centre general circulation model. *Atmos.–Ocean,* **33,** 407–446.

——, J. T. Kiehl, and P. J. Rasch, 1998: Response of climate simulation to a new convective parameterization in the National Center for Atmospheric Research Community Climate Model (CCM3). *J. Climate,* in press.